



UNIVERSITY OF LEEDS

This is a repository copy of *Independent and Hybrid Magnetic Manipulation for Full Body Controlled Soft Continuum Robots*.

White Rose Research Online URL for this paper:

<https://eprints.whiterose.ac.uk/199942/>

Version: Accepted Version

Article:

Abolfathi, K, Medina, JAR, Khaksar, H et al. (5 more authors) (2023) Independent and Hybrid Magnetic Manipulation for Full Body Controlled Soft Continuum Robots. *IEEE Robotics and Automation Letters*, 8 (7). pp. 4235-4242. ISSN 2377-3766

<https://doi.org/10.1109/lra.2023.3280749>

© 2023 IEEE. Personal use of this material is permitted. Permission from IEEE must be obtained for all other uses, in any current or future media, including reprinting/republishing this material for advertising or promotional purposes, creating new collective works, for resale or redistribution to servers or lists, or reuse of any copyrighted component of this work in other works.

Reuse

Items deposited in White Rose Research Online are protected by copyright, with all rights reserved unless indicated otherwise. They may be downloaded and/or printed for private study, or other acts as permitted by national copyright laws. The publisher or other rights holders may allow further reproduction and re-use of the full text version. This is indicated by the licence information on the White Rose Research Online record for the item.

Takedown

If you consider content in White Rose Research Online to be in breach of UK law, please notify us by emailing eprints@whiterose.ac.uk including the URL of the record and the reason for the withdrawal request.



eprints@whiterose.ac.uk
<https://eprints.whiterose.ac.uk/>

Independent and Hybrid Magnetic Manipulation for Full Body Controlled Soft Continuum Robots

Kiana Abolfathi, *Member, IEEE*, Jose A. Rosales Medina, Hesam Khaksar, James H. Chandler, *Member, IEEE*, Klaus McDonald-Maier, *Senior Member, IEEE*, Keyoumars Ashkan, Pietro Valdastrì, *Fellow, IEEE*, Ali Kafash Hoshidar*, *Member, IEEE*

Abstract— Fully soft continuum magnetic (FSCMs) microrobots with highly deformable structures have emerged as a potential solution to robotically controlled endovascular interventions. The microrobot's structure is made of magneto-responsive material, which offers full body control under a magnetic field instead of limited tip deformation. The shape control for these microrobots enables steering in complex paths with limited contact with the environment. We studied full body control under fields generated using up to two robotically controlled permanent magnets and in combination with an electromagnetic system. The effect of different parameters, such as the number of permanent magnets, position of the permanent magnets and intensity and direction of the electromagnetic field, on the robot's shape has been experimentally investigated. A mathematical model to predict tip deformation angle (TDA) was introduced and verified experimentally (root mean square error (RMSE) 6.5). Ten different characteristic body shapes were identified based on the curvature of the soft robot. Based on the obtained data, a proof-of-concept demo is presented for the full body controlled soft robots. The accuracy of steering soft robots on a continuous path with all three magnetic control strategies was investigated. The results show that the proposed method effectively enables shape forming and minimizes contact with the surrounding environment (the average distance to the centerline was 1.24 mm). The proposed approach hold promises to elevate endovascular interventions towards the least invasive surgery.

Index Terms—fully soft continuum magnetic (FSCMs) microrobots, magnetic control, shape forming, body shape control, microrobot, magneto responsive material.

I. INTRODUCTION

In recent years, microrobots have shown promising results in advancing existing medical interventions and introducing novel least invasive surgical procedures [1, 2]. To control microrobots, a wide variety of actuation methods have been introduced, including chemical, piezoelectric [3] and optical [4]. However, given its clinical compatibility, magnetic field actuation has emerged as the favored method for medical interventions involving microrobots.

Real-time information on the robot's location and orientation during surgery is important. MRI and X-ray can be used to

create a 3D map of the patient's anatomy to guide surgeries [5]. Additionally, soft magnetic robots have been used with imaging systems for real-time localization, and preliminary results suggest that embedded sensing devices like FBGs could also achieve real-time magnetic catheter localization [6, 7].

A specific subset of magnetic microrobots featuring a high aspect ratio (length-to-diameter) are particularly well suited to endovascular interventions, due to their soft (non-invasive), dexterous (highly deformable) and miniaturized (reaching to remote areas) structures. These small (milli/micro-scale) soft continuum magnetic (SCM) robots, driven by a high number of degrees of freedom and the ability to generate complex curvilinear shapes, have emerged as novel tools in the advancement of medical interventions.

SCM robot consists of a flexible structure with single or multiple embedded permanent magnets (PM) at their tip [8, 9], with variable stiffness, and with concentric tube configurations [10, 11].

To capture the behavior of SCM robots under magnetic fields, models have been proposed based on Cosserat rod theory [12], Kirchhoff elastic rod model [13], Pseudo Rigid Body Models (PRBMs) [14, 15], as well as finite element method (FEM) models [8, 9]. Despite compelling results, early SCM robots utilized rigid permanent magnets inside their soft structures, which present an increased risk of patient discomfort and potentially tissue damage of vascular perforation.

To address this limitation of SMC robots, fully soft continuum magnetic (FSCM) robots were introduced [16, 17]. These robots are fabricated from an elastomer matrix doped with magnetic microparticles (ferromagnetic magneto responsive material), resulting in an entirely soft, fully deformable structure with increased tip deformation and reduced the risk of tissue damage. The Euler-Bernoulli non-linear model was introduced for FSCM robots in [16], and a large deformation model presented in [18]. The microrobots are modeled as cantilever beams that are activated through an external magnetic field. By solving the boundary value problem

This work is supported by the University of Essex, Faculty of Health and Science, Department of Computer Science and Electronic Engineering, Robotics and Embedded System (RES) research group. Research reported in this article was supported by the Engineering and Physical Sciences Research Council (EPSRC) under grants number EP/R045291/1 and EP/V009818/1, and by the European Research Council (ERC) under the European Union's Horizon 2020 research and innovation programme (grant agreement No 818045). Any opinions, findings and conclusions, or recommendations expressed in this article are those of the authors and do not necessarily reflect the views of the EPSRC or the ERC. K McDonald-Maier's work was in part supported by UK EPSRC grants EP/V000462/1 and EP/X015955/1.

K. Abolfathi, H. Khaksar, J. A. R. Medina, K. McDonald-Maier and A. K. Hoshidar are with the School of Computer Science and Electronic Engineering, University of Essex, Colchester, CO4 3SQ, UK
*A.Kafashhoshidar@Essex.ac.uk

J. H. Chandler, P. Valdastrì, are with the STORM Lab, Institute of Autonomous Systems and Sensing, School of Electronic and Electrical Engineering, University of Leeds, LS2 9JT Leeds, U.K.

K. Ashkan is with the Department of Neurosurgery, King's College Hospital, SE5 9RS, London, UK

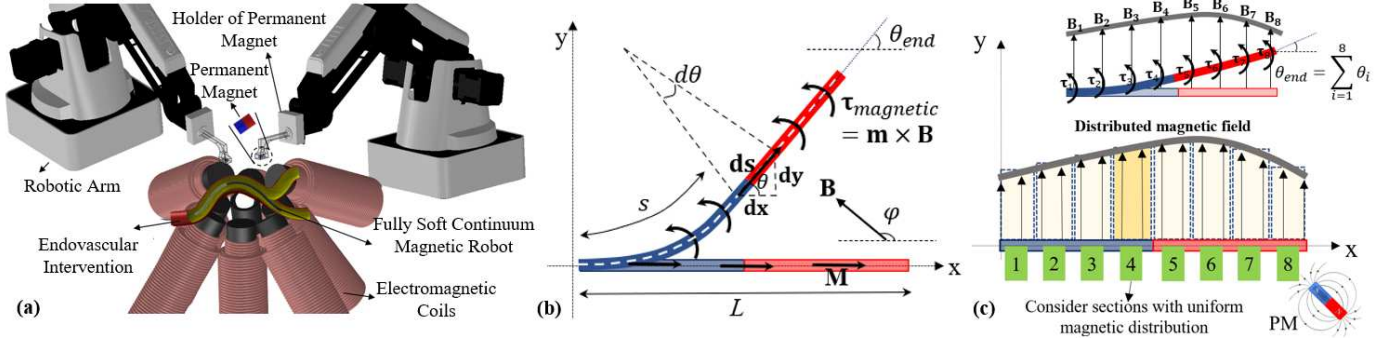


Fig. 1. (a) Schematic representation of magnetic field manipulation system for FSCM robot control under a magnetic field. (b) Schematic representation for FSCM robot deformation under a magnetic field. (c) Dividing the soft robot to different segments (each section has a uniform magnetic field)

using numerical methods and the Euler-Bernoulli beam equations, accurate determinations of the overall deformations can be obtained [19]. Additionally, the exact solution of the equations can be utilized to predict both the tip and shape deformations of these robots [20].

Approaches for shape forming of FSCM robots were introduced for actuation under static homogeneous fields [21] and for follow-the-leader navigation under sequenced homogeneous magnetic fields [22]. Fundamentally, these approaches achieve shape forming through the introduction of varied magnetization directions along the length of the FSCM robot, resulting in a varied response when exposed to a uniform magnetic field. Although shape forming to a specified shape or path was achieved, the approach is limited by fabrication complexity and each FSCM robot being specifically programmed to suit only one shape or path.

Permanent magnets have high magnetic energy density and, if mounted on robotic manipulators (RM), can provide a reconfigurable (and large) workspace [23, 24]. Additionally, electromagnetic coils have the advantage of controlling field intensity by modulating the current, thus providing an additional degree of control that allows fine tuning [25]. This paper's primary contribution lies in its exploration of a hybrid approach (Fig. 1 (a)), showing how we can get the best of both techniques (separately and together). For the first time, we demonstrate the advantages of fine-tuning control through EM coils while also leveraging the flexible workspace that can be achieved through the use of RMs.

Furthermore, we apply our hybrid approach for the shape control of the soft microrobots (diameter 600 μm with uniform axial magnetization) that expands beyond the limitation of tip control. Our experimental results showed that using only one magnetic source is limiting for full body shape control, while two simultaneously controlled magnetic sources facilitate this goal. We explore and evaluate the different pairings of three independent magnetic systems (two PM based and one EM depicted in Fig. 1 (a)) to achieve full body shape control for contact avoidance in a proof-of-concept study.

II. MODELING

A. Magnetic field modeling

To develop the model, we incorporated a range of assumptions that considered both the physical characteristics of

the microrobot and the behavior of its constituent materials:

- Given the microrobot's significant aspect ratio, with its diameter notably smaller than its length, the robot's cross-sectional area remains perpendicular to its centerline.
- The length of the centerline of the microrobot remains constant during deformation.
- The microrobot's material is modeled as isotropic and elastic [23].
- In the EM system, the magnetic field is considered uniform.
- To determine tip deformation angle under PM, we divide the soft robot into several segments, each with a uniform magnetic field (Fig. 1 (c)).

According to Maxwell's equations, the magnetic field is described:

$$\nabla \cdot \mathbf{B} = \mu_0 \mathbf{J} \quad (1)$$

$$\nabla \times \mathbf{B} = 0 \quad (2)$$

where \mathbf{B} is the 3×1 magnetic field, μ_0 is the permeability of free space, which is $4\pi \times 10^{-7} \text{ T}\cdot\text{A}\cdot\text{m}^{-1}$, \mathbf{J} is a vector field describing the electrical current density. According to equation (1), in a current free space the curl of the magnetic field is zero. The force and torque on a magnetic object under the effect of this magnetic field is thereby given by the following:

$$\boldsymbol{\tau}_{\text{magnetic}} = \mathbf{m} \times \mathbf{B} \quad (3)$$

$$\mathbf{F}_{\text{magnetic}} = (\mathbf{m} \cdot \nabla) \mathbf{B} \quad (4)$$

where $\mathbf{F}_{\text{magnetic}}$ and $\boldsymbol{\tau}_{\text{magnetic}}$ are 3×1 vectors and \mathbf{m} is the dipole moment of the magnetic object. As equations (3) and (4) illustrate, the magnetic torque depends on field (intensity and direction) and the magnetic force depends on field gradient.

Magnetic force and torque can be integrated into a 6×1 matrix [26]:

$$\begin{bmatrix} \boldsymbol{\tau}_{\text{m}} \\ \mathbf{F}_{\text{m}} \end{bmatrix}_{6 \times 1} = [\mathbf{M}]_{6 \times 8} [\mathbf{B}]_{8 \times 1} \quad (5)$$

where \mathbf{M} is the dipole term and \mathbf{B} is the magnetic field term.

\mathbf{M} can be shown as:

$$[\mathbf{M}]_{6 \times 8} = \begin{bmatrix} 0 & -m_z & m_y & 0 & 0 & 0 & 0 & 0 \\ m_z & 0 & -m_x & 0 & 0 & 0 & 0 & 0 \\ m_y & m_x & 0 & 0 & 0 & 0 & 0 & 0 \\ 0 & 0 & 0 & m_x & m_y & m_z & 0 & 0 \\ 0 & m_x & 0 & 0 & m_x & 0 & m_y & m_z \\ -m_z & 0 & m_x & -m_z & 0 & m_x & -m_z & m_y \end{bmatrix} \quad (6)$$

\mathbf{B} can be shown as:

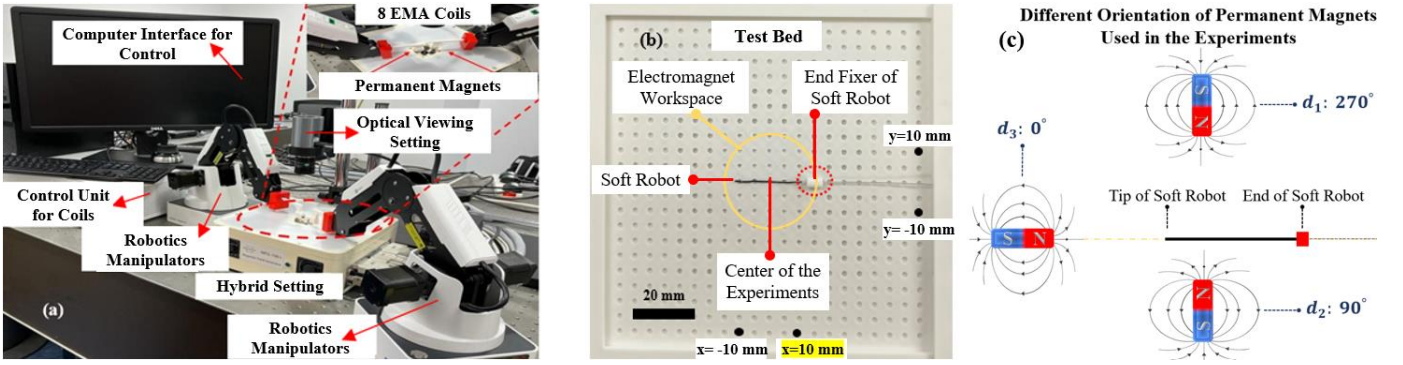


Fig. 2. Experimental set-up. (a) The hybrid navigation system which consists of two RMs and EM (b) The soft magnetic robot in the test bed. (c) Different orientation of the permanent magnet used in the experiments.

$$[\mathbf{B}]_{8 \times 1}^T \quad (7)$$

$$= \left[B_x \quad B_y \quad B_z \quad \frac{\partial B_x}{\partial x} \quad \frac{\partial B_x}{\partial y} \quad \frac{\partial B_x}{\partial z} \quad \frac{\partial B_y}{\partial y} \quad \frac{\partial B_y}{\partial z} \right]$$

In the presented study, the magnetic field (\mathbf{B}) is generated using RMs, EM or a combination of them. For the RMs, we use cylindrical shaped (N50, 3.5×7 mm) axially magnetized permanent magnets. Instead of approximating the field generated by the cylindrical magnets with a dipole model, we instead consider an ideal solenoid model. This approach uses a generalized complete elliptical integral, which naturally occurs in a field with cylindrical symmetry (at any given point in cylindrical coordinates $\mathbf{P} = (z, \rho, \phi)$) [27]. The EM field was considered uniform in the region of experiment.

B. Bending deformation modeling

We consider the tip deformation of a FSCM microrobot under a magnetic field; presented as a general schematic in Fig. 1(b). Where in Fig.1(b), s is the distance from the origin to the spatial point of interest (initial point of $d\mathbf{s}$), θ is the bending angle, \mathbf{B} is magnetic field, \mathbf{M} is magnetization in undeformed shape, \mathbf{m} is magnetization in deformed shape, A is the cross-section, φ is magnetic field direction, and θ_{end} is the final bending angle of the robot.

The curvature of the centerline ($c(s)$) can be calculated as eq.8 (Fig. 1(b)):

$$c(s) = \frac{d\theta}{ds} = \theta_s' \quad (8)$$

We can show the magnetic potential energy (ψ_m) and the bending energy per volume (ψ_b) as Eq. 9 and Eq. 10 [18].

$$\psi_m(\theta, s) = -\mathbf{R}\mathbf{M} \cdot \mathbf{B} \quad (9)$$

$$\psi_b(\theta') = \frac{EI}{2A} \theta'^2 \quad (10)$$

where \mathbf{R} is rotation tensors, E is the Yong modulus, and I is the area moment of inertia. Helmholtz free energy density (ψ_t) is a function of three variables (θ', θ, s).

$$\psi_t(\theta', \theta, s) = \frac{EI}{2A} \theta'^2 - \mathbf{R}\mathbf{M} \cdot \mathbf{B} \quad (11)$$

Based on eq.11, the total Helmholtz free energy can be calculated as eq.12.

$$\Pi(\theta_s) = A \int_0^L \psi_t(\theta', \theta, s) ds \quad (12)$$

Due to the principle of stationary potential energy $\delta\Pi = 0$, and using Eq.9 and Eq.10, and uniformity of the magnetic field

($\mathbf{F}_{\text{magnetic}} = (\mathbf{m} \cdot \nabla)\mathbf{B} = \mathbf{0}$), we have (Boundary value problem (BVP)) [23]

$$\frac{EI}{A} \frac{d^2\theta}{ds^2} + \mathbf{M}\mathbf{B}\sin(\varphi - \theta) = 0 \quad (13)$$

Based on Eq. 13 and using chain rule:

$$\int \frac{d^2\theta}{ds^2} \frac{d\theta}{ds} = - \int \frac{\mathbf{M}\mathbf{B}\mathbf{A}}{EI} \sin(\varphi - \theta) d\theta \quad (14)$$

There is no internal bending moment at the free end. Hence in Eq. 14, the boundary condition is $\theta'_{end} = 0$. Finally, , Eq. 15 shows the relation between bending angle and the length.

$$ds = \sqrt{\frac{EI}{2\mathbf{M}\mathbf{B}\mathbf{A}}} \frac{d\theta}{\sqrt{\cos(\varphi - \theta_{end}) - \cos(\varphi - \theta)}} \quad (15)$$

By integration from Eq.15:

$$L = \sqrt{\frac{EI}{2\mathbf{M}\mathbf{B}\mathbf{A}}} \int_0^{\theta_{end}} \frac{d\theta}{\sqrt{\cos(\varphi - \theta_{end}) - \cos(\varphi - \theta)}} \quad (16)$$

where L is the length of the soft robot. Based on Eq. 16 and the fact that the length of the soft robot remains constant, the final bending angle of the robot (θ_{end}) can be calculated by numerically solving Eq. 16 (using MATLAB software).

To calculate the bending angle of each segment under PM, the microrobot is divided into multiple sections, and the magnetic field distribution is approximated. The bending angle for each segment can then be determined, and the superposition method is used to obtain the overall tip deformation angle of the soft robot. The model parameters introduced in [21] is used in this study.

III. SOFT MAGNETIC ROBOT FABRICATION

The FSCM microrobots were fabricated using a two-part process. Magnetic tips were first made from neodymium-iron-boron (NdFeB) particles ($5 \mu\text{m}$ MQFP-B+, Magnequench GmbH, Germany) mixed with an elastomer (Ecoflex-0030, Smooth-On Inc, USA) in a 1:1 mass ratio.

After mixing and degassing in a vacuum mixer (ARV-310, THINKYMIXER, Japan) for 90 seconds at 1600 rpm and 20 kPa, the composite was injected into cylindrical moulds with cavity dimensions of $600 \mu\text{m}$ diameter \times 80 mm length. After curing at room temperature for a minimum of four hours, with no particle aggregation observed during this process, the magnetically doped elastomer was subsequently demolded and cut to the desired length of 25 mm.

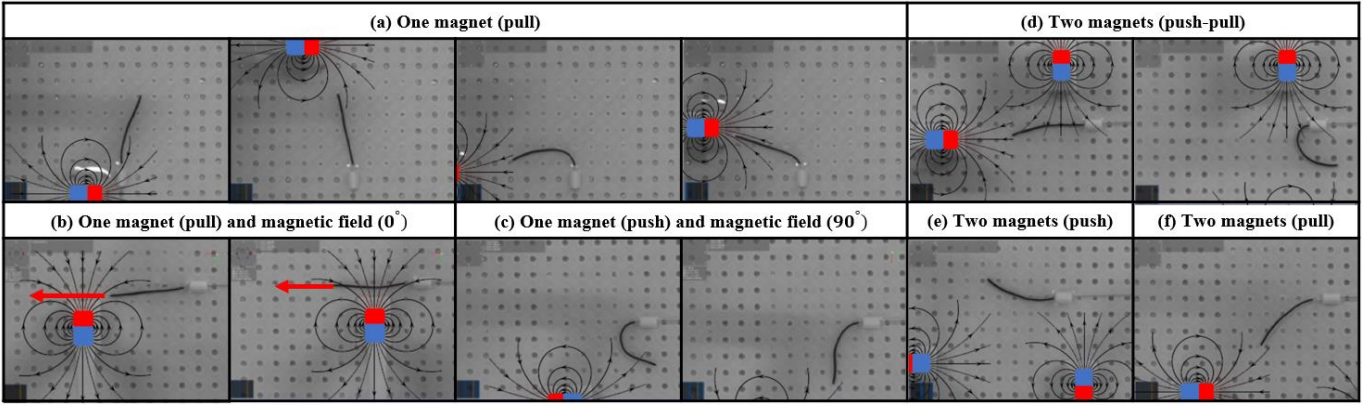


Fig. 3. Direction of electromagnetic field in image (b) is shown with red arrows. The position and orientation of the PMs are depicted with blue and red colors. The black field lines illustrate an approximate direction of the magnetic moment. The distinct body patterns of the soft robot which are shown under the effect of (a) One permanent magnet with pull effect and without the effect of EM field. (b) One permanent magnet and EM field with EM field direction at 0° . (c) One permanent magnet and EM magnetic field, (EM fiend intensity 1 mT at 90° direction). (d) Two permanent magnets with a pull and push effect. (e) Two permanent magnets with a push effect. (f) Two permanent magnets with the pull effect.

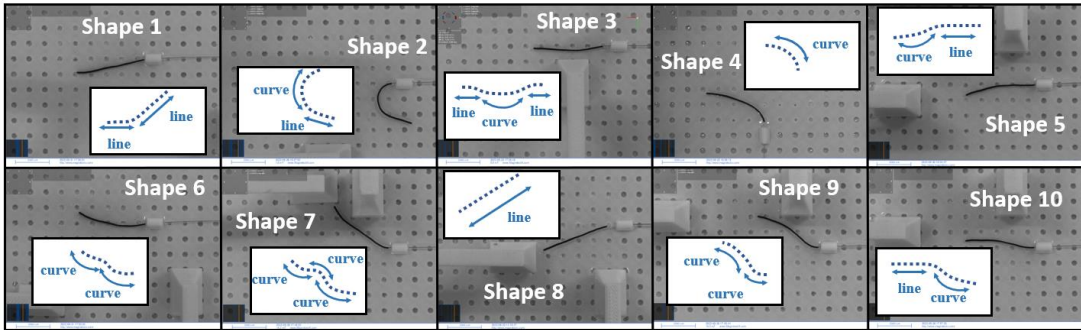


Fig. 4: Body pattern is classified based on combination of curve (nonlinear) and linear parts to ten different categories.

Sections were subsequently placed into an alignment fixture and magnetized in an axial direction using an impulse magnetizer (ASC IM-10-30, ASC Scientific, USA) to establish the soft robot's magnetic polarization (north/south poles) direction. In the second stage of fabrication, magnetized tips were bonded to a 100 mm length of flexible silicone microtubing (0.6 mm OD x 0.3 mm ID, McMaster-Carr, USA) using silicone adhesive (Sil-PoxyTM, Smooth-On Inc, USA). A nickel titanium wire of 0.25 mm diameter was inserted into the tube to further increase the stiffness of the proximal section of the catheter with respect to the magnetic tip.

IV. SOFT MAGNET ROBOT CHARACTERIZATION AND EXPERIMENTAL SETUP

A. Experimental setup

The experimental setup, including a magnetic field generator (MFG100), two robotics arms (DoBot Magician) and optical camera (Basler, puA1280-54um) for monitoring, is presented in Fig. 2(a). The MFG100 accurately generate and visualize real-time magnetic fields at the center of workspace. For each robot arm, a magnet holder was designed, and 3D printed to securely hold a Permanent Magnet (PM). Each robotic arm has $200 \mu\text{m}$ spatial resolution and the EM generator (MFG100), can produce a desired magnetic field within a spherical workspace of 30 mm diameter. The full body control is achieved using RMs (up to 2 magnets), or a combination of EM (field generator $<20 \text{ mT}$) and RM (hybrid method).

For the experimental tests, a phantom with $120 \times 120 \text{ mm}$ (width and length) was 3D printed (Fig. 2(b)). The platform is positioned to have a congruent center with the EM. The soft robot was positioned at this location for the experiments (shown in Fig. 2(b)).

To vary the magnetic field, the position of the RMs were changed inside the workspace in 5 mm incremental steps in the x and y directions (as illustrated by the grid pattern in Fig. 2(b)) with or without the addition of EM fields. To limit data collection, redundant scenarios were ignored.

Full body shape control was investigated in three different scenarios: First, the full body control with one RM (Fig. 3(a)), two RMs (Fig. 3(d) to (e)) and hybrid EM and RM actuation (Fig. 3(b) and (c)). The supplementary video shows these three-test configuration. From these experimental results, the behavior of the FSCM robot was classified into ten main body shapes (Fig. 4), each considered based on resulting curved and linear features. The following sections consider each scenario and corresponding shapes achievable in detail.

B. RM controlled soft robot

The FSCM (Fig. 2) has North and South poles. Therefore, depending on the orientation of the PMs (position of north and south poles), they can push or pull the FSCM robot. The different combinations of push-pull states were considered as detailed in the following two sections. The orientation and direction for the PM(s) in each scenario is fixed.

1) One Permanent Magnet (PM)

Three assumptions for the presented experiments were considered. 1) The effect of the PM on the shape of the FSCM robot in the upper half of the test bed is considered symmetrical with that of the lower half. Consequently, the effect of the PM is studied only on one side of the test bed. 2) For one PM, the effect of push and pull are considered similar. 3) Cases where the FSCM robot touches the PM holder are considered invalid and any corresponding FSCM robot shape is disregarded. 4) The orientation of the PM is d_2 Fig. 2(c).

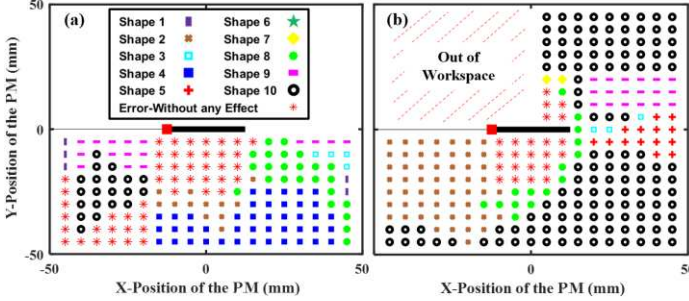


Fig. 5. Phase diagram of the FSCM robot's shape under effect of (a) One RM in different positions. (b) Two RMs when the location of one RM is fixed and the position of the other changes. The first RM with a push-configured PM was fixed at position: $(x,y) = (-5 \text{ mm}, 10 \text{ mm})$.

For each valid position of RM, the FSCM robot's shape was classified using a polynomial function (10th order). An image processing algorithm (MATLAB, MathWorks, USA) was developed, to detect the pixels containing the FSCM robot and thus its position within the workspace. The results were utilized to construct a straight line passing through the microrobot's center and its tip. The difference between set points for y and x (in pixels) was calculated from the image and used to determine the tip deformation angle (TDA) parameter as:

$$\text{TDA} = \tan^{-1}\left(\frac{dy}{dx}\right) \quad (17)$$

where, dy and dx are distance in y and x directions respectively. The TDA is used to quantitatively classify different shape types.

Seven shapes (1, 2, 3, 4, 8, 9, and 10) with TDA ranging from $\{-1.89, 13.31, -0.43, 5.83, 2.38, -6.69, \text{ and } -2.380^\circ\}$ to $\{3.17, 22.45, 1.37, 20.94, 13.60, 0.93, \text{ and } -1.01^\circ\}$ were generated for PM positions across the workspace under the pulling configuration, as shown in Fig. 5(a). The results show that although using one PM allows the generation of different shapes, the variation in achievable TDA was limited. Issues with single PM tests include attachment between the RM and FSCM for close PM positions (high fields) and a loss of shape forming efficacy for larger distances from the center of workspace. The range shapes possible using one RM are limited for full body shape control. Consequently, generation of more body shapes is essential.

2) Two Permanent Magnets (PMs)

For the two RMs, three different scenarios were considered: pull-push, pull-pull, and push-push.

a) RM Push-Pull permanent magnets:

In this series of experiments, the RM with a push-configured PM was moved between two points with (x, y) equal to $(-5 \text{ mm}, 10 \text{ mm})$ and $(5 \text{ mm}, 10 \text{ mm})$. The other RM, with a pull-configured PM, was moved across the entire workspace. The full body shape patterns of the FSCM robot while the push-configured RM was positioned at $(-5 \text{ mm}, 10 \text{ mm})$ are presented in Fig. 5(b). Moreover, the orientation of the push and pull pm are states d_1 and d_3 (Fig. 2(c)) respectively. This shows seven body shape patterns (2, 3, 5, 7, 8, 9, and 10) with TDAs ranging from $\{-176.50, -18.80, -59.35, -24.34, -31.61, -23.05, \text{ and } -24.34^\circ\}$ to $\{175.92, 42.09, -37.18, -20.22, 112.31, -6.448, \text{ and } 119.54^\circ\}$. Compared to the one PM, a new shape (5) was observed.

The experiment was repeated with the position of the fixed RM moved to position $(x, y) (5 \text{ mm}, 10 \text{ mm})$. The shape pattern

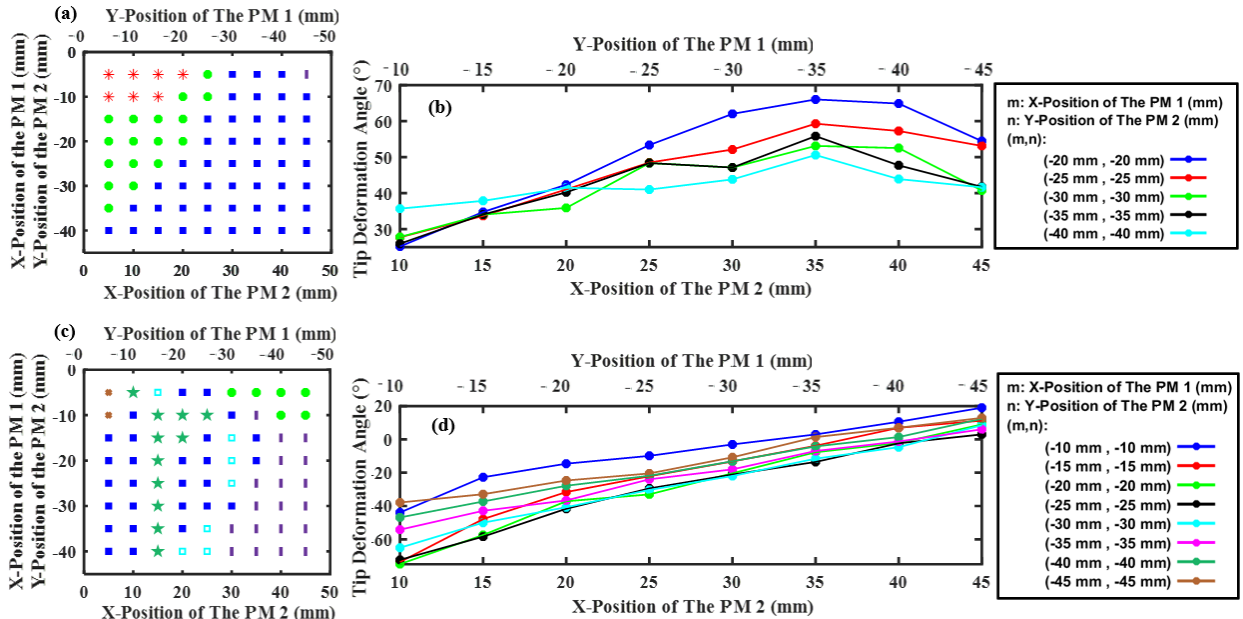


Fig. 6. (a) Phase diagram of different patterns of soft robot in different positions of RMs when both arms hold PM with pull effect. (b) TDA over positions of RMs, when both arms hold PM with pull effect. (c) Phase diagram of different patterns of soft robot in different positions of RMs, when both arms hold PM with push effect. (d) TDA over positions of RMs when both arms hold PM with push effect.

distribution showed 81% similarity to the results presented in Fig. 6; with shape differences primarily observed in the close proximity to the fixed RM. A mean variation in TDA of 4.13% was found. The maximum and minimum variation were 18.45° and 1.04° respectively.

b) RM Pull permanent magnets:

With both RMs in pull-configurations, their positions were changed within a specific range. The first RM was moved between -40 to -5 mm in the x-direction and between -5 to -45 mm in the y-direction (Fig. 2(b)) and with orientation of d_3 (Fig. 2(c)). The second RM was moved between 5 to 45 mm in 5 mm incremental steps in the x-direction (supplementary video), and from -40 to -5 mm in the y-direction and with orientation of d_2 (Fig. 3(c)). The polynomial function representing the shape was determined for each location across the workspace (Fig. 6(a)). The variation in TDA is presented in Fig. 6(b), where one RM is considered stationary and the other moves between 10 to 45 mm. As seen in Fig. 6(a), the RM with two push-configured PMs generates three different body shapes (1, 4 and 8) with TDA ranging from $\{17.45, 34.04 \text{ and } 23.55^\circ\}$ to $\{17.45, 84.17 \text{ and } 49.97^\circ\}$ respectively. This scenario shows an extend range of TDA in shape 4 and 8 from 5.83 to 20.24 to 34.04 and 84.17 respectively.

c) RM Push permanent magnets:

The RM settings for this experiment was similar to the two RM tests with pull-configured PMs; resulting in similar trend in TDA. The body shape distribution and TDA are presented in Fig. 6(c) and (d) respectively. For this test case, 6 body shapes were generated; shapes (1, 2, 3, 4, 6, and 8), with TDAs ranging between $\{-1.25, -73.61, -20.41, -72.35, -41.63, \text{ and } 10.62^\circ\}$ and $\{12.93, -43.88, -7.70, 3.01, -22.11, \text{ and } 19.03^\circ\}$. According to the results, the range of the TDAs was expanded for shapes 1 and 2, and a new shape (shape 6) was observed in this scenario.

3) Hybrid control of soft robot

To steer the FSCM robot under contact free conditions through a vascular phantom, it is critical to minimize dynamic transitions between shapes. To achieve this objective, it is necessary to produce different shapes with an extended range of controllable TDAs. A hybrid actuation approach (EM and RM) was tested to allow fine tuning of the magnetic field and thus to increase the range of TDA in some of the body shapes for improved mitigation of dynamic transitions between the shapes. The orientation and direction of the PM(s) in section (a) and (b) are d_3 and d_2 (Fig. 2(c)) respectively.

a) Variable magnetic field strength

To investigate the effect of the field intensity on TDA and the body shapes, an EM generated magnetic field between 0 to 15 mT was studied. The TDA for different positions of the one RM (with a pull-configure PM) for different EM magnetic field conditions is shown in Fig. 7(a) and Fig. 7(b).

The results in Fig. 7 illustrate that without EM fields, the effect of PM on the shape of soft robot is dominant. However, in the presence of an EM field, the PM can be located closer to the FSCM without attachment. This enables precise tip movement, eliminating jumps in the motion of the FSCM robot.

Three outputs can be observed from the results. (1) The TDA changes with RM for movements in the y-direction show a

similar (declining) trend and the x position of RM and EM intensity effects the shape pattern. (2) In each x-position series, there is a specific value of EM strength, that reduces the TDA below 2° . (3) The x position of the RM defines the effective range value of the EM field.

For positions with x equal to 30, 40, and 45 mm, when y changes between -5 and -45, the TDA is almost zero for EM magnetic field values greater than 3 mT.

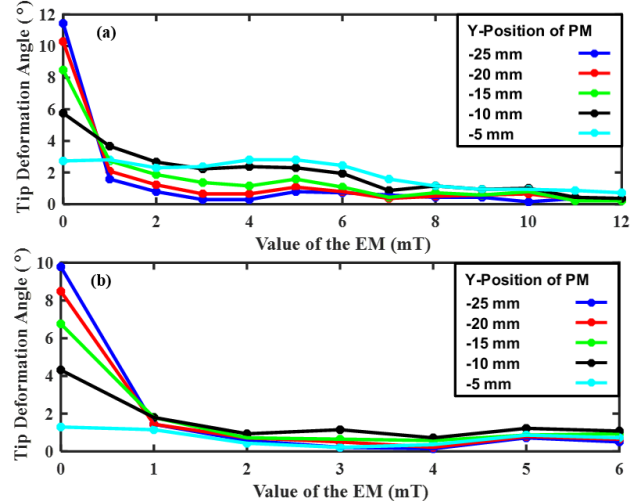


Fig. 7. Tip deformation angle (TDA) over the different value of EM in a hybrid system (RM with pull-configured PM and EM). (a) RM fixed in x direction at 20 mm and y changed between -25 mm and -5 mm. (b) RM fixed in x direction at 25 mm and y changed between -25 mm and -5 mm.

Precise control of the TDA is crucial in preventing abrupt shifts in the soft robot's body shape. When examining the EM-RM field conditions indicated by squares in Figure 8, we observe a significant impact from the RM in the absence of an EM field. However, the presence of EM enabled fine-tuning of the soft robot tip.

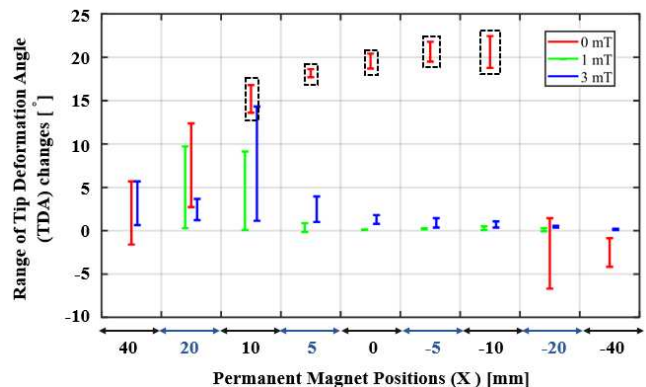


Fig. 8. Range of FSCM robot's tip deformation angle (TDA) in different positions of the permanent magnet under EM field (0, 1, and 3 mT)

b) Magnetic Field in 90° Direction

In addition to EM field magnitude, we also considered field direction for both 0° (as detailed in the previous section) and 90° in this section.

The position of a RM was changed in x and y direction from 5 to 40 mm and from -30 to -10 mm, respectively. Also, all magnetic field conditions (strength and direction) are assumed similar (1 mT at 90° direction). The results of these experiments are illustrated in Fig. 9. Using the hybrid scenario, in shape 2 the TDA could be changed precisely (ranging between 17.91 to 19.50°).

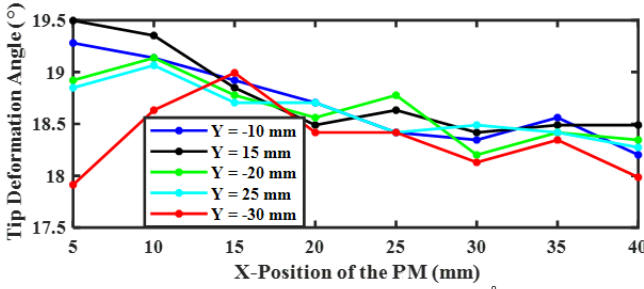


Fig. 9. TDA changes in the hybrid field with EM field at 90° and 1 mT intensity.

V. MODEL COMPARISON WITH EXPERIMENTS

A comparison between the experimental results and the developed model (Eq. 16) is presented in Fig. 10. For this comparison, the FSCM robot was exposed to the magnetic field generated by a RM (with a pull configured PM). EM generated fields of 2 mT, 5 mT, and 10 mT were subsequently imposed. The measured and model predicted TDA values are compared in Fig. 10. The developed model shows agreement with experimental data, demonstrating estimation of tip-deformation in the presence of a RM and EM field separately and simultaneously. A root mean square error (RMSE) of 6.5 between simulation and experiments is observed.

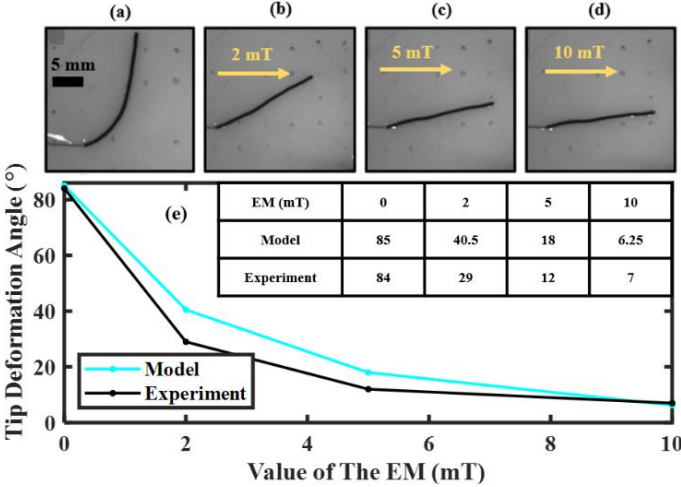


Fig. 10. Comparison between the simulation and experimental (RM and RM/EM) results.

VI. PROOF OF CONCEPT STUDY

As an illustrative application of body shape control, we developed a proof-of-concept study to demonstrate full body control along a 2D path (radius 3 mm shown in the supplementary video). In the first step, the path is divided into N segments. As the aim was to deliver rectilinear motion and body shape control simultaneously, the length of each segment was dynamically changed. Each segment was designed to optimize the rectilinear motion of the FSCM robot without contacting the boundary. Depending on the specific requirements, the selection of the field used to generate the body shapes was based on both the model (TDA prediction) and experimental data (estimated shape).

The path structure was recorded using a camera for pre-planning purposes. Subsequently, the path was segmented into a set of shapes that the FSCM robot can achieve. Each segment

was also assigned a start and end position. For this experiment, 14 discrete steps were obtained.

The FSCM robot was attached to a manual introducer and moved sequentially through these 14 segments. Using the data set created (for shape type shown in Fig 2 and 3) and field models (for tip deformation angle), the magnetic conditions (position of permanent magnets and values of EM magnetic field) were obtained for each segment. For simplicity in this demonstration, the positions were registered to the experimental test bed and a manual approach in PM placement was used (supplementary video). Three repeats for each scenario were implemented.

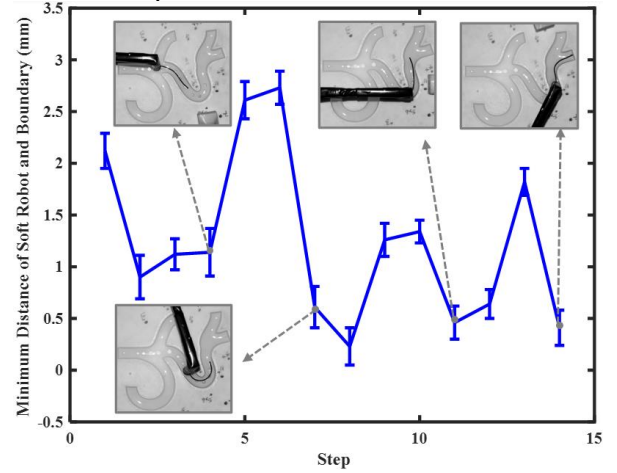


Fig. 11. The minimum distance between the FSCM and vessel boundary ($n=3$ after three experiments). The picture of experiment for four segments (4, 7, 11, and 14) is shown.

The accuracy of these tests was investigated by measuring the minimum distance of the FSCM robot to the boundary of the path at each stage. An ideal distance of the soft robot to the wall, for a perfectly centered configuration, is 3 mm. Therefore, the minimum distance can range between 0 to 3 mm. An average (mean) minimum distance for each repeat was 1.24, 1.27, and 1.21 mm. The minimum distance between the FSCM robot and the vessel boundary across each step is demonstrated in Fig. 11.

VII. CONCLUSION

In this study, a novel hybrid magnetic manipulation approach for shape forming of soft robots based on the combined use of PM and EM field generation has been proposed. Up to ten different body shapes were generated, forming a wide range of possible TDAs. Moreover, a model was presented to predict TDAs under hybrid field conditions and this showed agreement with experimental results (RMSE 6.5).

The effect of different modes (one PM, two PM, hybrid actuation) on shape forming was studied and a large range of experimental data was obtained. In general, modes with only PM(s) produced a diverse set of shapes, while EM schemes enhanced the range TDAs possible for given shapes. This variety in shape and tip control enabled precise shaping of the FSCM robot through a phantom vasculature without contact and with an average minimum robot-wall distance of 1.24 mm. This approach has the potential to enable improved navigation in delicate anatomy at small scales, reducing risk to the perforations, improving current endovascular procedures, and opening new opportunities towards the ultimate goal of “least invasive surgery”.

The orientation of the permanent magnet (PM) has been considered as a constant parameter (0° , 90° and 270°). However, this parameter can influence the tip deformation angle (TDA). As such, the future work needs to further extend the orientation scenarios. In addition, a potential direction for future work could be to model shape forming under the hybrid approach.

REFERENCES

- [1] A. Moghanizadeh, H. Khaksar, and A. Hoshiar, "A novel non-invasive intervention for removing occlusions from shunts using an abrading magnetic microswarm," *IEEE Transactions on Biomedical Engineering*, 2022.
- [2] D. Li, M. Jeong, E. Oren, T. Yu, and T. Qiu, "A helical microrobot with an optimized propeller-shape for propulsion in viscoelastic biological media," *Robotics*, vol. 8, no. 4, p. 87, 2019.
- [3] Y. Chen *et al.*, "Controlled flight of a microrobot powered by soft artificial muscles," *Nature*, vol. 575, no. 7782, pp. 324-329, 2019.
- [4] S. Palagi, D. P. Singh, and P. Fischer, "Light-controlled micromotors and soft microrobots," *Advanced Optical Materials*, vol. 7, no. 16, p. 1900370, 2019.
- [5] J. Hwang *et al.*, "An Electromagnetically Controllable Microrobotic Interventional System for Targeted, Real-Time Cardiovascular Intervention," *Advanced Healthcare Materials*, vol. 11, no. 11, p. 2102529, 2022.
- [6] F. Khan, A. Denasi, D. Barrera, J. Madrigal, S. Sales, and S. Misra, "Multi-core optical fibers with Bragg gratings as shape sensor for flexible medical instruments," *IEEE Sens. J.*, vol. 19, no. 14, pp. 5878-5884, 2019.
- [7] C. M. Heunis, F. Šuligoj, C. Fambuena Santos, and S. Misra, "Real-time multi-modal sensing and feedback for catheterization in porcine tissue," *Sensors*, vol. 21, no. 1, p. 273, 2021.
- [8] S. Jeon *et al.*, "A magnetically controlled soft microrobot steering a guidewire in a three-dimensional phantom vascular network," *Soft robotics*, vol. 6, no. 1, pp. 54-68, 2019.
- [9] A. Kafash Hoshiar, S. Jeon, K. Kim, S. Lee, J.-y. Kim, and H. Choi, "Steering Algorithm for a Flexible Microrobot to Enhance Guidewire Control in a Coronary Angioplasty Application," *Micromachines*, vol. 9, no. 12, p. 617, 2018.
- [10] Y. Piskarev *et al.*, "A Variable Stiffness Magnetic Catheter Made of a Conductive Phase-Change Polymer for Minimally Invasive Surgery," *Adv. Funct. Mater.*, p. 2107662, 2022.
- [11] Q. Peyron *et al.*, "Magnetic concentric tube robots: introduction and analysis," *The International Journal of Robotics Research*, p. 02783649211071113, 2022.
- [12] J. Edelmann, A. J. Petruska, and B. J. Nelson, "Magnetic control of continuum devices," *The International Journal of Robotics Research*, vol. 36, no. 1, pp. 68-85, 2017.
- [13] L. B. Kratchman, T. L. Bruns, J. J. Abbott, and R. J. Webster, "Guiding elastic rods with a robot-manipulated magnet for medical applications," *IEEE Transactions on Robotics*, vol. 33, no. 1, pp. 227-233, 2016.
- [14] R. J. Roesthuis and S. Misra, "Steering of multisegment continuum manipulators using rigid-link modeling and FBG-based shape sensing," *IEEE transactions on robotics*, vol. 32, no. 2, pp. 372-382, 2016.
- [15] V. K. Venkiteswaran, J. Sikorski, and S. Misra, "Shape and contact force estimation of continuum manipulators using pseudo rigid body models," *Mechanism and machine theory*, vol. 139, pp. 34-45, 2019.
- [16] Y. Kim, G. A. Parada, S. Liu, and X. Zhao, "Ferromagnetic soft continuum robots," *Science Robotics*, vol. 4, no. 33, p. eaax7329, 2019.
- [17] Y. Kim *et al.*, "Telerobotic neurovascular interventions with magnetic manipulation," *Science Robotics*, vol. 7, no. 65, p. eabg9907, 2022.
- [18] L. Wang, Y. Kim, C. F. Guo, and X. Zhao, "Hard-magnetic elastica," *J. Mech. Phys. Solids*, vol. 142, p. 104045, 2020.
- [19] W. Chen, Z. Yan, and L. Wang, "On mechanics of functionally graded hard-magnetic soft beams," *International Journal of Engineering Science*, vol. 157, p. 103391, 2020.
- [20] W. Chen and L. Wang, "Theoretical modeling and exact solution for extreme bending deformation of hard-magnetic soft beams," *Journal of Applied Mechanics*, vol. 87, no. 4, p. 041002, 2020.
- [21] P. Lloyd *et al.*, "A learnt approach for the design of magnetically actuated shape forming soft tentacle robots," *IEEE Robotics and Automation Letters*, vol. 5, no. 3, pp. 3937-3944, 2020.
- [22] P. Lloyd, G. Pittiglio, J. H. Chandler, and P. Valdastrì, "Optimal design of soft continuum magnetic robots under follow-the-leader shape forming actuation," in *2020 International Symposium on Medical Robotics (ISMR)*, 2020: IEEE, pp. 111-117.
- [23] G. Pittiglio, M. Brockdorff, T. da Veiga, J. Davy, J. H. Chandler, and P. Valdastrì, "Collaborative Magnetic Manipulation via Two Robotically Actuated Permanent Magnets," *IEEE Transactions on Robotics*, 2022.
- [24] G. Pittiglio *et al.*, "Patient-Specific Magnetic Catheters for Atraumatic Autonomous Endoscopy," *Soft Robotics*, 2022.
- [25] J. Hwang *et al.*, "An Electromagnetically Controllable Microrobotic Interventional System for Targeted, Real-Time Cardiovascular Intervention," *Advanced Healthcare Materials*, p. 2102529, 2022.
- [26] A. J. Petruska and B. J. Nelson, "Minimum bounds on the number of electromagnets required for remote magnetic manipulation," *IEEE Transactions on Robotics*, vol. 31, no. 3, pp. 714-722, 2015.
- [27] N. Derby and S. Olbert, "Cylindrical magnets and ideal solenoids," *Am. J. Phys.*, vol. 78, no. 3, pp. 229-235, 2010.